

Crater Identification in Chang'E 5 landing sequence

Vasilis Michalakis

The University of Adelaide

a1887068@adelaide.edu.au

Tat-Jun Chin

The University of Adelaide

Sentient Satellites Lab

tat-jun.chin@adelaide.edu.au

ABSTRACT

Crater identification is the process of matching observed craters in space with those in a predefined catalogue. It is crucial towards the development of more accurate navigation on planetary bodies. The current state-of-the-art Lost in Space method maximizes the number of numerical descriptors representing camera-pose-independent features of a crater constellation, to facilitate their matching. We evaluate this method by matching crater detections from the Chang'E 5 landing sequence against the most comprehensive crater catalogue, the Robbins Database. We find this process yielded unverifiable, inconsistent matches when using both a reprojection test against catalogued craters and a vote-and-identify process for match verification.

1 INTRODUCTION

Chang'E 5 (CE5) is a Chinese National Space Agency (CNSA) robotic lunar sample return mission launched in November 2020 [1]. Image data obtained from the descent phase is of high quality and therefore valuable towards further research in Crater Identification (CID) methods.

CID is the process of using conventional cameras to observe craters on planetary bodies and match them with records in a predefined crater catalogue [2]. As part of the CID pipeline, images with crater observations are first processed through a Crater Detection Algorithm (CDA), where ellipses are fitted to the rims of detected craters [3].

CID solutions can be broadly categorized into two classes: tracking and Lost in Space (LiS) [2]. Tracking algorithms utilize a known priori state (i.e., camera pose [position and orientation]) to project catalogued craters onto an observed image and compare ellipse parameters [2, 3]. Alternatively, LiS matching operates on the premise that limited priori information is available [2, 3]. This paper focuses on LiS matching, as the crater detection dataset from the Chang'E 5 (CE5) landing sequence lacks camera pose information from the descent.

The current state-of-the-art LiS CID method proposed by Christian et al. leverages invariant theory to maximize the number of descriptors (camera-pose-independent features) of crater constellations to facilitate their matching [2]. Using human-labelled crater detections from the CE5 descent [4], this paper aims to evaluate the prediction stability of this method in identifying identical craters across successive frames, utilizing a subset of the largest crater catalogue, the Robbins Database [2, 5]. Note, the scope of this work excludes evaluating CDAs, and evaluates stability given the absence of ground truth IDs.

1.2 Motivation

The motivation for researching CID methods arises from practical use in Terrain Relative Navigation (TRN) systems. The adoption of TRN helps reduce propellant wastage during descents by facilitating more autonomous landings [6]. This decreases reliance on communication with a ground station and the associated lags that lead to inefficiencies [6]. Additionally, areas of greater scientific interest are often closer to hazardous terrain requiring a landing precision approximately 100m from target [6]. A TRN can achieve this precision, whereas current inertial guidance systems may produce inaccuracies of up to 10km [6]. Aside from TRN, crater identification can be utilized to streamline the process of registering scientific images [2].

The motivation for this research stems from the understanding that no other paper has evaluated the method proposed by Christian et al. on crater detections from the CE5 descent [2, 7]. Notably, Rodda et al. highlight that this is likely the first annotated dataset of crater detections for the CE5 landing sequence and of real lunar images with off-nadir viewing angles [8]. Furthermore, there appears to be a gap regarding the evaluation of the stability of Christian et al.'s method for identifying identical craters across successive frames. [2, 7].

2 LITERATURE REVIEW

There are a variety of LiS CID methods that can be used to identify craters in the CE5 landing sequence.

2.1 Deriving invariants from points of intersection

Park et al. proposed a method inspired by the application of planetary landings [9]. This method utilizes the matching of crater triangles [9].

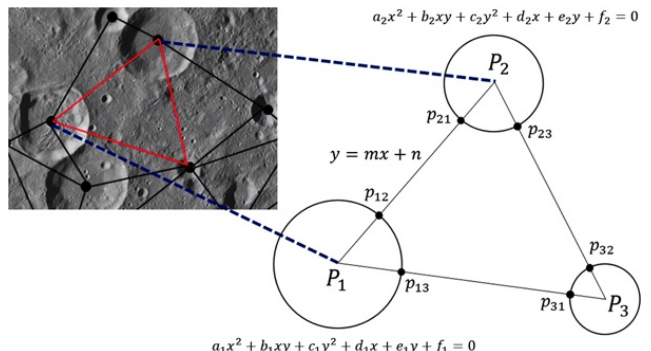


Figure 1 crater triangle to compute projective invariants [9]

As seen in figure 1, each crater rim is twice intersected by the triangle perimeter. For each of the six intersections, a five-element perspective and permutation invariant (p^2) vector is constructed using five points of coplanar intersections [9]. These six sets of five p^2 invariant vectors generate a 30-element descriptor [9]. Since the crater rims may not be coplanar, Park et al. employ coplanar approximation that projects the non-coplanar crater rims onto a common plane to determine the points of intersection (refer to A.1.1) [9]. Following this, for each observed crater triad, their matching algorithm calculates the Euclidean distance between the descriptors of the observed triad and all triads within the descriptor database [9]. Their algorithm then selects the pairs with the smallest distances, and if the distance is below a certain threshold, the matched crater triangle is verified through a voting system [9]. This system randomly selects one matched crater triangle, while the remaining matches "vote" on the number of identified occurrences of each crater [9]. Any crater receiving votes above a specified threshold is considered a verified match, which helps reduce false positives [9]. However, this verification process requires the CDA to detect a sufficient number of craters to form multiple triangles, which diminishes matching rates when craters are sparse [9]. Furthermore, the thirty-element descriptor contains only four independent invariants, leading to inefficient memory usage without adding discriminative power [2, 7].

2.2 Deriving invariants from surface normal vectors

In contrast, Maass et al. propose several crater identification techniques, but their Lost-in-Space (LiS) method is of particular interest [3]. Assuming circular crater rims and the validity of the pinhole camera model, two possible normal vectors exist for each crater, one of which is the surface normal that intersects the projected cone, whose curve forms the detected ellipse on the image plane (refer to A.1.2) [3]. For multiple detected craters, this leads to 2^n possible configurations [3]. A global optimization approach is used starting with three nearby craters and extending to more, selecting the configuration that minimizes surface curvature energy [3]. The final configuration provides relative depth estimates for the craters, constrained by the assumption of a smooth lunar surface [3]. Since only relative crater distances are determined, a comparison must be conducted using invariants [3]. Maass et al. form a descriptor pair using the interior angles of a crater triad (refer to A.1.3) [3]. Using the k -vector method, an initial hypothesis of three matches is formed for a constellation of craters [3]. The interior angles of nearby craters are compared to the existing constellation, allowing for the expansion of the hypothesized set to include five craters [3]. With this set of hypothesized matches, a camera pose can be estimated using the Efficient Perspective-n-Point (EPnP) method to compare the centres of the reprojected catalogue craters [3]. First, assuming craters are circular often leads to errors in the projective invariants, as many small craters are elliptical, causing inaccuracies in the estimated surface normal [2]. Second, the current pattern descriptor uses fewer parameters, missing key pieces of information impeding descriptive power [2]. Lastly,

verifying crater matches using only crater centers requires more craters [2], diminishing matching rates when craters are sparse.

2.3 State-of-the-art descriptor method

Christian et al. proposed a descriptor-based LiS CID method that matches constellations of craters. Leveraging invariant theory, they maximize the number of unique invariants that describe a crater constellation [2]. Christian et al. recognize CID as a multi-scale pattern recognition problem, classifying craters as local (coplanar) and global (non-coplanar) [2]. For non-coplanar craters, triads of craters are considered, where the planes of three conics intersect at a point a_{ijk} [2]. The pairwise intersection of the planes form three lines, for which two are coplanar with each plane (and therefore conic) and converge at a_{ijk} (figure A.1.4) [2].

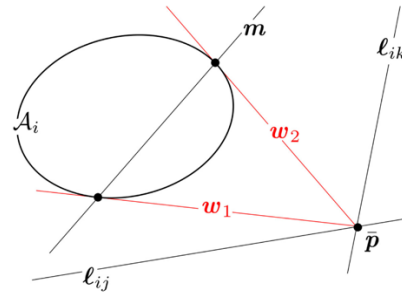


Figure 2 non-coplanar cross-ratio invariant [2]

As seen in figure 2, the use of the coplanar lines l_{ij} , l_{ik} and tangents w_1, w_2 from the conic (to the intersection of the coplanar lines \bar{p}) yields four points on a line (m) for which the cross-ratio can be calculated [2]. Using the Cayley-Klein metric, an invariant can be computed to form a descriptor element [2]. Hence, for a non-coplanar crater constellation of size d , the maximum number of unique projective invariants is $3d - 6$ ($n \geq 3$) [2]. For a pair of coplanar conics, there exist four points of intersection and two invariants: by calculating the cross ratio of the lines from four intersection points to an arbitrary point on the first conic and to an arbitrary point on the second conic (refer to A.1.8) [2]. These descriptor elements are calculated using a rational function of this cross-ratio as it is more computationally efficient [2]. Therefore, for a coplanar crater constellation of size d , there exist $5d - 8$ unique invariants ($n \geq 2$) [2]. To construct a crater catalogue from a list of known craters, Christian et al. proposed utilizing HEALPix regions to constrain the formation of crater constellations, thereby limiting both the number of combinations and the size of the catalogue while enabling the inclusion of more craters from different regions (refer to A.1.5) [2]. These constellations are stored in a k-d tree or n-d k vector [2]. To determine match hypotheses, Christian et al. proposed three methods for constructing a pattern descriptor: matching invariants in an unordered vector by searching the catalogue for each permutation of a constellation, pre-sorting the invariant vectors (e.g., by crater size) to match with a single search, or matching the p^2 invariant descriptors [2]. For each hypothesis, camera attitude is then used to estimate a camera pose [2]. Finally, the match is

verified by using the estimated pose to reproject the candidate match from the crater catalogue onto the image plane and determine the difference using a Gaussian Angle (GA) distance metric (refer to A.1.6) [2]. If below a threshold value, the hypothesis is considered a valid match ending the verification process [2]. Chng et al. highlight that a major weakness of this method is the susceptibility of the descriptors to noise in the observed ellipse parameters, which can reduce matching rates or lead to false positive matches [7]. Additionally, the rapid growth in catalogue size ($\binom{n}{d}$) for n craters with constellation size d constrains the use of additional invariant descriptors to improve accuracy [7]. Furthermore, large catalogues (e.g. Robbins database) may require pruning (i.e. HEALPix) to fit in memory, which can result in loss of crater coverage [7].

2.4 Descriptor-less LiS matching

Chng et al. proposed a descriptor-less LiS CID method based on the Perspective Cone Alignment (PECAN) problem which estimates relative camera position by aligning the projections of observed craters with back-projection conics in the image plane (refer to A.1.7) [7]. By assuming known camera orientation, global camera positions are derived from the estimated relative positions and crater centers in the catalog [7].

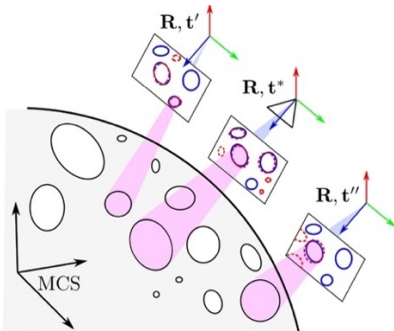


Figure 3 PECAN CID matching using estimated pose [7]

As shown in Figure 3, catalogue craters are projected onto the image plane as blue ellipses and compared with observed parameters represented by red ellipses using Euclidean distance. If the distance is below a specified threshold, the craters are considered a match [7]. The goal of this method is to determine the camera pose parameter (t^* in Figure 3) that maximizes the number of identified craters and returns the identified set [7]. Chng et al. assert that their method has linear time and space complexity relative to catalogue size, allowing the entire Robbins database to be utilized as a crater catalogue without the need for pruning [7]. This is particularly significant, as prior methods are unable to achieve this [2, 3, 9]. However, this CID method relies on camera attitude within the matching algorithm, which limits its applicability in scenarios where the camera attitude is unknown. Hence, this method cannot be applied to the crater detections in the CE5 landing sequence.

3 METHODOLOGY

The method proposed by Christian et al. uses attitude to verify matches by estimating the camera pose for conducting a reprojection test [2]. To ensure compatibility with the dataset, we propose two adapted methods. Additionally, our implementation searches the crater catalogue by forming a descriptor for each permutation of a constellation for matching.

Vote and Identify

Since the method proposed by Christian et al. matches crater constellations rather than individual craters, a single crater is likely to be represented in multiple constellations. As a result, when matching constellations, the ID of that individual crater may differ across matched constellations. To address this, we employ a vote-and-identify mechanism. For an individual crater appearing in various permutations of crater constellations, the majority predicted ID is returned. It is important to note that we do not apply a threshold value to the majority class to exclude predictions with lower confidence.

Pose estimation using Perspective-n-Pose

In our method, we match the descriptors of an observed constellation with the crater catalogue. We then estimate the camera's extrinsic matrix and its location in the world coordinate system using the SQPnP algorithm [10]. The intrinsic matrix is known; therefore the estimation depends on the correspondence between the x, y coordinates of the crater centres in the 2D image plane and the x, y, z coordinates of the predicted catalogue match in the world coordinate system. Proceeding this, we reproject the predicted matches and calculate the GA between the reprojected ellipses. If the reprojections of all craters in the constellation are below the threshold value, the remaining observed craters are matched using nearest neighbours. Our rationale for this approach is that we can predict only one pose per frame. We initiate nearest neighbour matching by first excluding catalogue craters outside the field of view, performing a reprojection check to ensure that their centre coordinates are visible within the frame. Next, we verify the visibility of the remaining craters relative to a sphere (representing the moon). This process begins by establishing a line connecting the camera's position to the sphere. We then solve a quadratic equation to determine that the crater centre does not lie on the opposite side of the sphere (moon) or behind the camera, by checking the smallest root approximately matches the length of this line. Next, for each pair of observed craters and visible catalogue craters, we compute the GA of the reprojected catalogue crater. This is then sorted so that the pairs of matched craters that minimize the GA are identified as the nearest neighbours. If these pairs are below a threshold, they are considered matches. Finally, if a user-defined percentage of the observed craters are matched successfully, the set of matches is returned, and the craters are deemed to match for that frame. Otherwise, we first explore a different match hypothesis, followed by a different crater constellation permutation. If we exhaust all constellations for a frame without finding a match, no match is identified for that frame. Alternatively, in dense regions of crater detections, we establish a timeout to terminate the identification process for a frame if no matches are found. This is illustrated in figure 4.

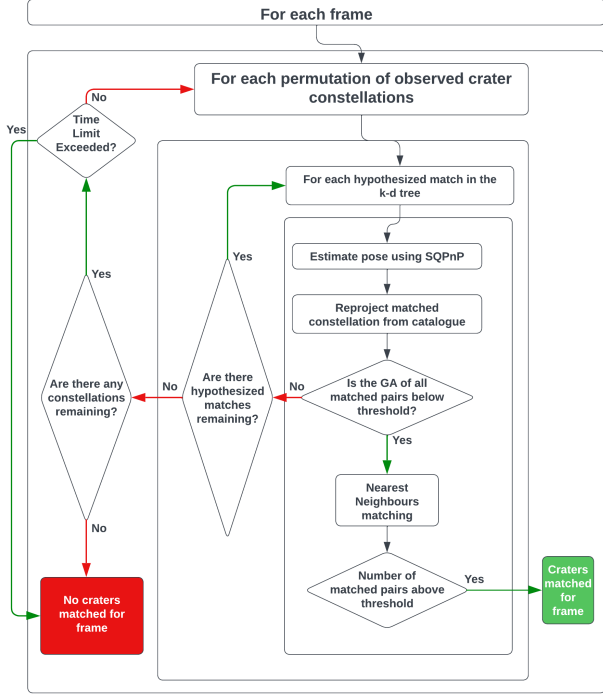


Figure 4 Flow diagram of our PnP method

4 EXPERIMENTAL SETUP

4.1 Descriptor database (crater catalogue)

Choosing a subset of the Robbins Crater Catalogue

Based on the estimated landing trajectory (refer to A.2.2), the descent phase can likely see craters from longitudes 280° to 310° and latitudes 35° to 45° [11]. We filter craters with ellipse centres located between longitudes 285° and 320° and latitudes 30° and 50° to account for potential visibility outside the initial range due to the viewing angle. We start at 285° longitude because no craters in the first frame matched the Digital Elevation Map by Yang et al. at 280° longitude [11].

Filtering craters from the subset

We further filter the subset to select locally visible craters with diameters between 0 and 30 km, ensuring that at least 90% of their rims are traced, resulting in a catalogue of 2,540 craters.

Constellation sizes

A constellation size of 3 craters was used, meaning descriptors were computed from triads of craters, ensuring ample coverage of the landing region, without requiring excessive pruning.

Computing descriptors

We compute descriptors under the assumption that the craters are coplanar. Our rationale is based on the fact that the descent phase of CE5 begins at an altitude of around 15 km above the lunar surface [11], whereas Christian et al. conducted experiments using

coplanar descriptors from an altitude of 150 km [2]. Hence, we compute seven-element descriptors.

HEALPix

Our catalogue requires the use of HEALPix as $(^{2540}_3)$ crater triangle combinations are too numerous to fit in memory. We opt to use 32 nside regions ($k = 5$ where $nside = 2^k$) as Christian et al. identify this as a useable resolution for local crater matching [2]. This prunes the total number of combinations to 47,643,735.

4.2 Processing the input

Grouping identical craters across the landing sequence

The crater detections from all 132 frames were manually grouped to identify identical craters throughout the landing sequence. We refer to these identical craters throughout the sequence as “tracked craters”. The dataset is labelled for every frame from image 0 to 100, and every 10th frame from image 100 to 413.

Modifications to the ellipse parameters

The ellipse parameters for the dataset were provided in the format $[x, y, a, b, \psi]$ (refer to A.2.1). In the labelled data, these values are scaled between a range of 0 to 100 relative to the image coordinate system. Our method also requires rotation in radians, so the parameters must be adjusted using the formula:

$$[x \times \frac{\text{width}}{100}, y \times \frac{\text{height}}{100}, a \times \frac{\text{width}}{100}, b \times \frac{\text{height}}{100}, \psi \times \frac{\pi}{180}]$$

Where width and height are 2352 and 1728 pixels respectively.

4.3 CID Parameters of vote and identify method

Num sampled

This parameter represents the number of detected craters to select and identify for a given frame. We set it to 260 to ensure that all craters in every frame of the landing sequence are identified.

4.4 CID Parameters of PnP method

Number of hypothesized matches

This parameter represents the number of closest matches to the crater catalogue, which we set to 10. A hypothesized match is utilized to estimate the camera pose for a crater constellation permutation.

Matching rate

This parameter specifies that a certain percentage of detected craters must be identified through nearest neighbours matching relative to the total number of crater detections for a set of matches to be considered successful. We set this rate to 0.5.

Image sigma

Image sigma specifies the error in ellipse parameters in terms of pixels; we assume an error of 3 pixels. This parameter is used to adjust the GA distance metric for the amount of noise.

GA distance verification metric

We use metric $\frac{d_{GA}^2}{\sigma^2}$ (see to A.1.6) with a threshold of 13.277 as proposed by Christian et al to compare an observed ellipse against the reprojected ellipse [2]. We refer to this as the GA distance metric

Raw GA verification metric

We also employ an experiment using d_{GA}^2 (see A.1.6) as the verification metric for reprojected craters for which we set a threshold of 2.1. We refer to this as the raw GA metric.

Time limit

We impose a time limit of 1800 seconds (30 minutes) for iterating over the various permutations of crater triangles before concluding that no possible matches exist for a given frame.

Intrinsic Matrix

This parameter is used to estimate camera pose, which is crucial to the reprojection test. We use $f_x \approx 59^\circ$, $f_y \approx 45^\circ$, $c_x = 1164.01684$ and $c_y = 858.041$ [12] (refer to A.2.3).

4.5 Evaluation Metrics

Visualizing the frequency of majority ID predictions

In each frame, for every detected crater rim, we label the frequency of predictions for the majority ID. This shows the stability of prediction for all individual craters, allowing for comparison.

Plotting the distribution of confident majority IDs

A confident majority ID for a crater exists when half or more of the total predictions of a crater ID are for the majority ID. This is used to discard low confidence predictions and more importantly verify that craters are uniquely identified (i.e. two different craters are not assigned the same ID).

Plotting a consistency ratio

The consistency ratio measures the confidence of a prediction by measuring the ratio between the frequency of the majority ID and the number of labelled frames of an observed ellipse. This plot shows the confidence relative to other tracked craters.

Visualizing catalogue reproductions

In each frame, for every matched crater rim, we show the reprojected ellipse and connect it to the centre of the observed ellipse using a straight line. This visualization indicates the quality of the camera pose estimate but is also useful as an indirect indicator of match quality.

Plotting estimated camera position

The estimated camera positions (in world coordinates) for each frame can be plotted using the PnP CID method, alongside the matches from the vote and identify method (utilizing SQPnP). If the matches are accurate, the plot is expected to closely resemble the landing trajectory as visualized by Yang et al (refer to A.2.2) [11]. This serves as an additional verification step for the matches.

5 RESULTS

5.1 Our PnP method using GA distance metric

Of the 132 labelled frames in the landing sequence, our PnP method yielded predictions in frames 0 and 20. Consequently, this experiment failed to yield any meaningful results.

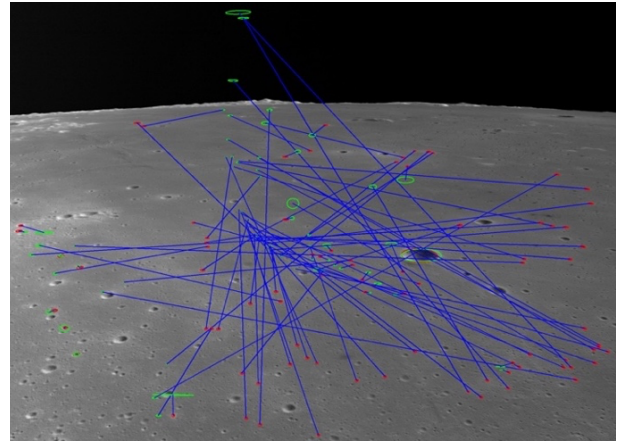


Figure 5 visualization of reprojection test in frame 20

In the figure above, the red ellipses denote the observed craters, whereas the green ellipses denote the reprojected craters. Upon inspection of figure 5, it becomes evident that the predicted matches are of low quality. Notably, the method seems to favour matching small craters. The fact that these match pairs fall below the GA distance threshold suggests either a potential issue with the threshold or the metric itself.

GA Distance metric experiment

To identify the source of the high reprojection error, we conduct an experiment simulating close and distant match pairs (reprojection ellipses) for both a small and a large observed ellipse. We use an ellipse detection error of $\sigma_{img} = 3$ pixels.

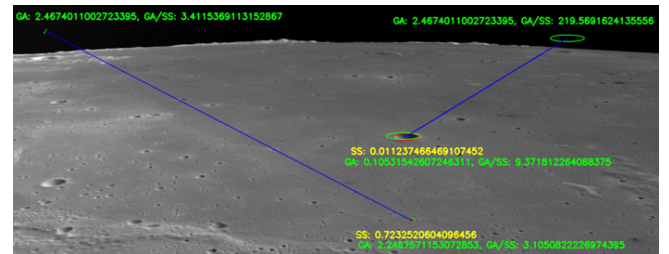


Figure 6 GA distance metric experiment

As illustrated above, the red ellipses represent the observed craters, while the green ellipses simulate the reprojected ones. Upon first glance, the GA distance metric appears flawed when matching small craters. The GA distance metric permits a close match pair for both small and large observed ellipses as expected. However, this metric (denoted GA/SS in figure 6) identifies the pair for the small observed ellipse as a significantly closer match.

When comparing distant match pairs, the GA distance metric exceeds the threshold for the large crater pair but remains significantly below the threshold for the small crater pair. Notably, this distance is less than the close match pair distance for the large ellipse.

This issue partially arises from the calculation of σ (see appendix A.1.6). This is because $\sigma \propto \frac{1}{\sqrt{a_i}}$ and $\sigma \propto \frac{1}{\sqrt{b_i}}$, where a_i and b_i are the lengths of the semi-major and semi-minor axes of the observed ellipses. Consequently, as the craters decrease in size, the semi-major and semi-minor axes become shorter, and the ellipse fit error (σ) increases. This is illustrated in Figure 6, which shows a higher σ^2 value for the smaller crater (denoted by SS in red text). Since $\sigma \propto \sigma_{img}$, merely adjusting σ_{img} is insufficient due to the vast range of crater sizes. Increasing σ_{img} to accommodate a greater ellipse fit error in larger craters will lead to additional false positive matches of smaller craters, while reducing σ_{img} (thereby reducing the ellipse fit error in smaller craters) will further reduce the number of large craters matched. Furthermore, the value of d_{GA} is asymptotically bounded as $d_{GA} \propto \arccos\left(\exp\left[-\frac{c}{2}\right]\right)$ (see appendix A.1.6).

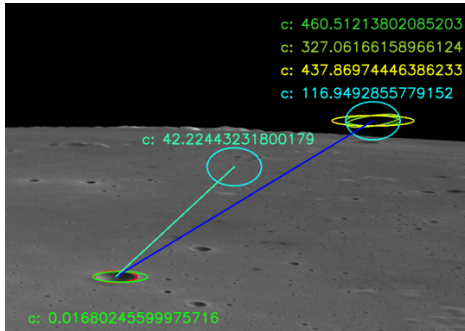


Figure 7 value of c relative to differing ellipse parameters

As the ellipse parameters differ, c increases (as shown in figure 7). Due to multiplication by scalar $-\frac{1}{2}$, the value within the exponential term decreases as parameters differ. Since $\lim_{x \rightarrow -\infty} e^x = 0$, we can therefore conclude that $\lim_{c \rightarrow \infty} e^{-\frac{c}{2}} = 0$. Therefore, the expression within the inverse cosine function ($e^{-\frac{c}{2}}$) is asymptotically bounded by 0, because of a multiplication by 0 (see appendix A.1.6). Hence, the asymptotic bound of d_{GA} is $\arccos(0) \approx 1.57$ rad or $d_{GA}^2 \approx 2.46$ rad. In Figure 6, this asymptotic value is reached for distant match pairs of both small and large crater observations, as the computed exponential is likely too small to be represented as a floating-point number, resulting in the computation of the inverse cosine of 0. These observations prompted us to conduct an experiment with our PnP implementation using d_{GA}^2 (raw Gaussian Angle) as the verification metric instead. Consequently, the low-quality matches in frames 0 and 20 can be attributed to the high prevalence of small craters in these frames, along with a verification metric that is ineffective for small craters in this case.

5.2 Our PnP method using raw GA metric

Using our PnP method with the raw GA metric, we returned a set of predictions for frames 80, 83–88, 270–290, 310–330, 380, 400 and 410. We consider these predictions as two separate segments, as the craters from frames 80 to 88 are not visible in the field of view for the sequence of frames from 270 to 410.

Frame sequence 80 to 88

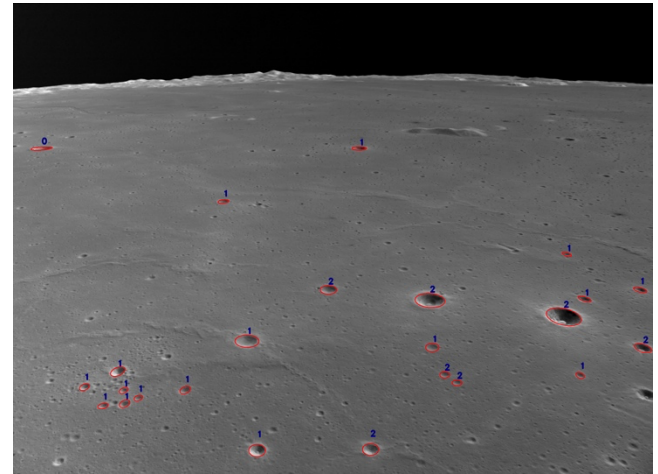


Figure 8 Frequency of majority ID predictions in frame 88

As illustrated in Figure 9, by the end of the first segment of matched frames, the majority IDs of identical craters were predicted no more than twice. Therefore, in this segment, matching a tracked crater with an ID in the Robbins catalogue is challenging, as the frequency of majority predictions is low relative to the number of frames, indicating low prediction confidence. This issue stems from the fact that a subset of matches were only returned for seven frames, limiting the number of individual predictions for a tracked crater, thus constraining the ability to find a pattern.

Frame Sequence 270 to 330

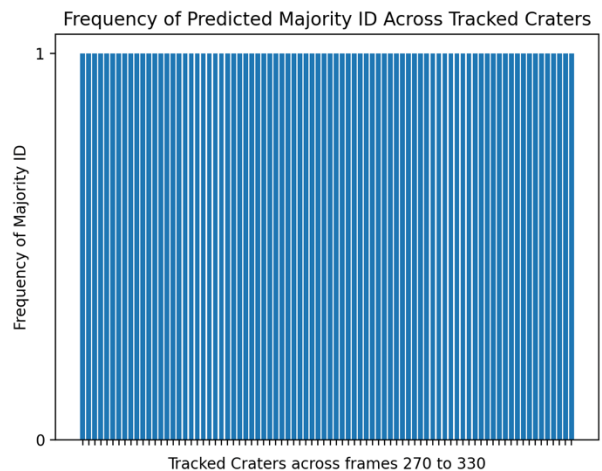


Figure 9 Majority ID frequency in frames 270 to 330

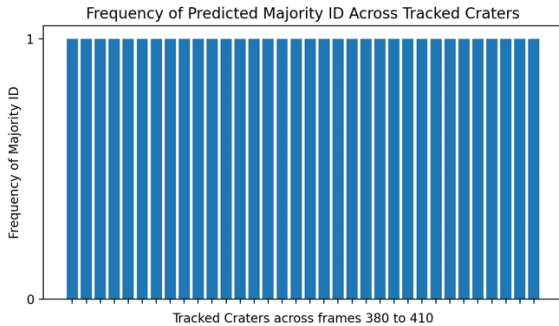


Figure 10 Majority ID frequency in frames 380 to 410

For each tracked crater in the sequence of frames 270-330 and 380-410, the majority ID was predicted no more than once (as illustrated by figures 9 and 10), meaning that a confident match could not be identified. It is worth noting that there are fewer visible ellipse observations for a tracked crater from frames 110-410 since labelling is conducted for every 10 frames. As mentioned previously, this constrains the number of individual predictions for a tracked crater across the sequence.

Reprojection test

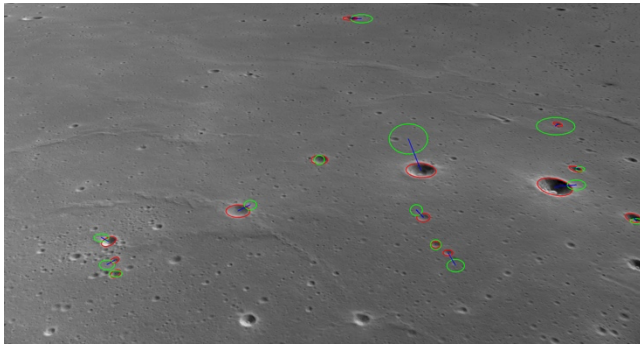


Figure 11 Reprojection test on frame 88

As shown in Figure 11, using the raw GA metric reduces the number of nonsensical small crater matches. Furthermore, the ability of this method to return a set of matches across multiple frames, where the GA distance metric fails (as the prevalence of small craters is lower), suggests that employing the raw GA metric may also increase the matching of larger craters.

Method limitations

Our PnP method starts with a random camera pose based on a randomly chosen crater triangle, leading to two main issues: accepting any match above the threshold without checking all permutations for the best match, and the inefficiency of testing all permutations. Hence, in this experiment, 115 frames in the landing sequence hit the 30-minute timeout before matching could complete. Given more time, some matches might have succeeded. To address this, in the next section we manually estimate global camera position using selected matches derived from the vote-and-identify method.

Furthermore, the off-nadir camera poses in frames 0 to 270 may challenge the coplanar assumption used in matching the descriptors. Assuming craters are coplanar when they are not

leads to descriptors that may not resemble projective invariants, which could explain the low stability in ID predictions, particularly across frames 80 and 83-88.

Finally, the estimated pose may be sub-optimal because it assumes that the 3D catalogue crater centre projects to the same centre as the 2D observed crater, which is not accurate for a non-nadir pose [13]. Since the estimated pose is crucial for nearest neighbour matching, the sub-optimal pose may contribute to reprojection errors, resulting in the high rejection of matches or false positives.

5.3 Vote and identify method

Running the vote and identify method yielded predictions for every labelled crater across all frames of the landing sequence. To determine the stability of matching, we plot the distribution of confidently predicted majority IDs of tracked craters visible in ten or more frames. Since this method permits repeated predictions for the same crater ID within a single frame, the plot provides insights into the uniqueness of each confident match.

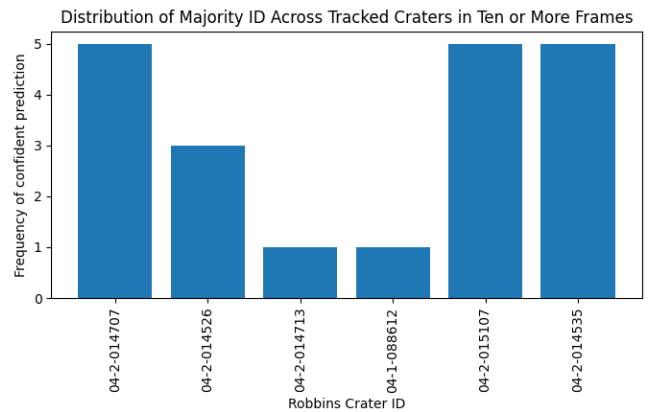


Figure 12 Majority prediction frequency

As illustrated above, there are several IDs for which a maximum of five tracked craters, appearing in ten or more frames, received the same confident majority prediction, indicating poor stability. For the two confident ID predictions where only one crater is matched to the catalogue, we choose to plot a consistency ratio.

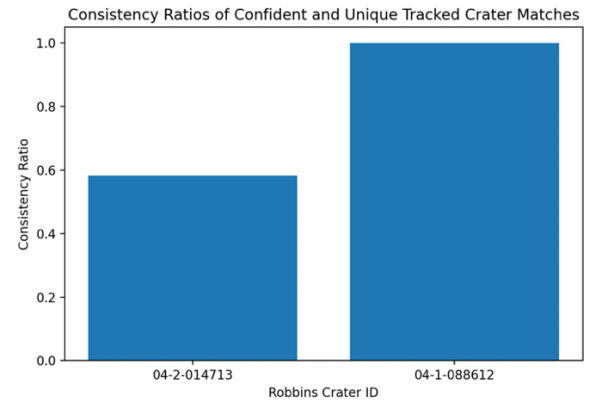


Figure 13 consistency ratios of unique confident predictions

As illustrated in Figure 13, a tracked crater with the predicted ID “04-1-088612” consistently matched to the same (unique) ID across all labelled frames. However, despite the stable prediction of this crater across all 38 labelled frames in the landing sequence, there remains the possibility that all matches are false positives. Hence, we decide to estimate and plot the camera position for each frame.

Plotting estimated camera position

To visualize the camera position for each frame, we first identify a subset of high-quality crater matches, requiring a minimum of three matches for each frame. Since we must utilize craters with ID clashes to form constellations that span the landing sequence, we ensure that these conflicting IDs are carefully considered. We iterate through all craters, counting how often the same ID appears in subsequent frames while allowing for two-frame intervals of ID variations. We then tally the frequency of the most prevalent pattern ID. In instances of ID clashes, we select the tracked crater with the higher prevalent pattern ID frequency. If the prevalent pattern ID frequencies are the same, we then prioritize the crater based on the majority ID frequency. This process will narrow down a concise list of unique craters, each with distinct IDs, forming our constellation. We cut this list to 10 craters. Within this constellation, if any crater’s ID prediction in the sequence of labelled frames differs from the prevalent pattern ID (or the majority ID, if they are the same), we will adjust it to ensure consistency. Next, we will construct crater triangles by prioritizing craters based on their highest pattern frequency, followed by majority ID frequency in cases where pattern frequencies are identical, particularly when the subset of craters exceeds three. It should be noted that this method will not find a constellation for every frame.

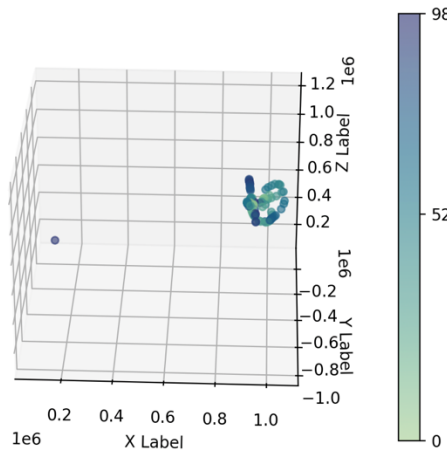


Figure 14 Estimated camera position for CE5 descent

As seen in figure 14, the estimated camera position does not appear to resemble the trajectory of the CE5 landing sequence as shown by Yang et al (refer to A.2.2) [11]. Consequently, the accuracy of the matches cannot be further verified, particularly regarding whether the tracked crater with the matched ID “04-1-088612” is a false positive, despite showing no deviations in predicted ID across the sequence.

6 CONCLUSION

The results of this project did not yield any verifiable matches with a subset of the Robbins database for crater detections in the CE5 landing sequence. To ensure compatibility with the dataset, we proposed two alternate verification mechanisms to Christian et al.’s method [2]. The first method employs a vote and identify mechanism based on permutations of crater triangles, while the second utilizes SQPnP to estimate camera pose from a matched triangle and a nearest neighbours algorithm to match the remaining catalogue against the observed craters in a frame. Experiments using our PnP method revealed that the GA distance metric proposed by Christian et al. [2] is ineffective for inputs with varying crater sizes. However, a set of consistent and verifiable matches was not produced. The vote and identify method returned a set of matches; however, the majority predicted IDs were not unique to most tracked craters, with the exception of one tracked crater that consistently received the same prediction across all labelled frames. When estimating and plotting camera location using a subset of high-quality matches, the camera trajectory did not align with the expected landing sequence trajectory, resulting in an inability to verify any of the predicted matches. Overall, this work concludes that the prediction stability of descriptor-based Lost-in-Space methods may be unreliable, particularly in true LiS scenarios where no pose information is available.

6.1 Future Work

There are several limitations in our experiments. One significant challenge involves the off-nadir camera poses in frames 0 to 270, which undermine the assumption of coplanarity among crater constellations used in descriptor matching. Future investigations should consider computing non-coplanar descriptors. Alternatively, labelling further frames beyond 270, where the camera achieves a nadir-viewing pose, could expand the set of detected craters in conditions more favourable for matching.

If both experiments yield no results, the subset of the Robbins database created for this project, along with a series of generated poses, can be utilized to create synthetic ellipse detections that simulate the CE5 descent with known correspondences. Subsequently, the same crater identification experiments can be conducted using both coplanar and non-coplanar descriptors to evaluate the method’s accuracy in matching craters.

7 LINK TO RELEASE

<https://github.cs.adelaide.edu.au/a1887068/CraterID/releases/tag/v1.0.0>

APPENDIX

A.1 Literature Review

A.1.1 Coplanar approximation proposed by Park et al.

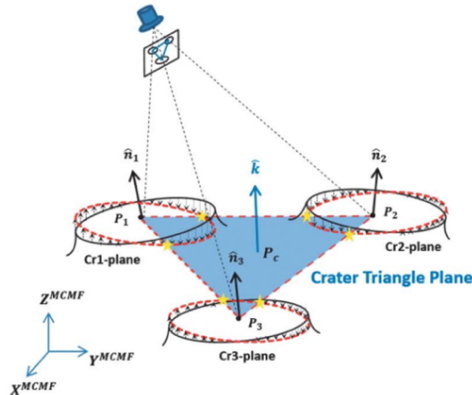


Figure A.1.1 Coplanar approximation by projection [9]

The illustration above depicts the coplanar approximation utilized by Park et al. whereby non-coplanar craters are projected on a common triangular plane from which intersections are decided.

A.1.2 Surface normal of circular crater

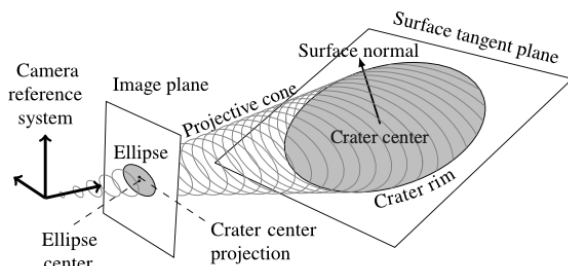


Figure A.1.2 Perspective projection of crater-rim [3]

The illustration above shows the surface normal vector intersecting the projected cone. The other normal configuration, which does not represent the surface normal, is a mirror image of the surface normal in the illustration.

A.1.3 Crater triangle invariants using interior angles

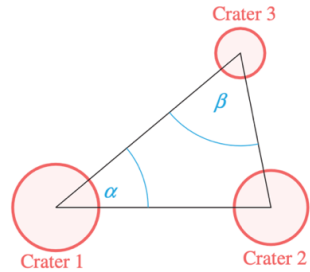


Figure A.1.3 crater triangle of interior angles [3]

The illustration above shows the interior angles of crater triangle (projective invariants) where α is the smallest angle and β is the middle angle.

A.1.4 Invariants of non-coplanar craters using coplanar lines

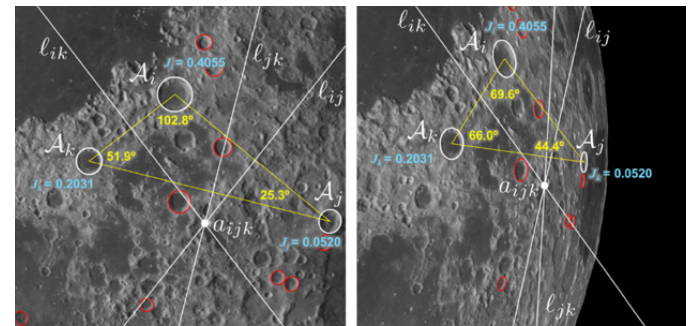


Figure A.1.4 Invariants from pairs of coplanar lines [2]

The illustration above shows the projected coplanar lines l_{ik} and l_{ij} which are coplanar to projected conic A_i in the 2D image plane. These are derived from 3D observations C_i (crater), L_{ij} and L_{ik} (coplanar pairs of lines).

A.1.5 Illustration of HEALPix

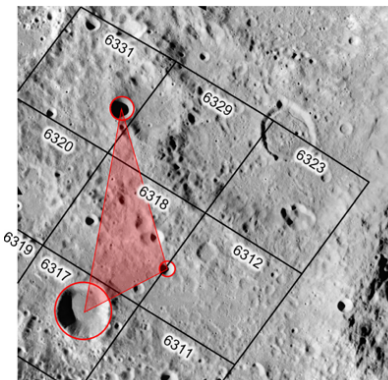


Figure A.5 3x3 HEALPix grid [2]

The illustration above shows how for each HEALPix grid around the reference pixel (6318 in this example), valid crater constellations (triads) are formed from the craters within the 3×3 grid.

A.1.6 Gaussian Angle distance metric used by Christian et al. [2]

Christian et al. define an approximation of the Gaussian Angle distance metric as

$$\frac{d_{GA}^2}{\sigma^2}$$

In the equation above d_{GA} is defined as

$$d_{GA} = \arccos \left(\frac{4\sqrt{|\mathbf{Y}_i||\mathbf{Y}_j|}}{|\mathbf{Y}_i + \mathbf{Y}_j|} \exp[-\frac{c}{2}] \right)$$

Where c is defined as

$$c = (\mathbf{y}_i - \mathbf{y}_j)^T \mathbf{Y}_i (\mathbf{Y}_i + \mathbf{Y}_j)^{-1} \mathbf{Y}_j (\mathbf{y}_i - \mathbf{y}_j)$$

Where \mathbf{Y}_i (and subsequently \mathbf{Y}_j) are defined as

$$\mathbf{Y}_i = \begin{bmatrix} \cos \psi_i & -\sin \psi_i \\ \sin \psi_i & \cos \psi_i \end{bmatrix} \begin{bmatrix} 1/a_i^2 & 0 \\ 0 & 1/b_i^2 \end{bmatrix} \begin{bmatrix} \cos \psi_i & \sin \psi_i \\ -\sin \psi_i & \cos \psi_i \end{bmatrix}$$

and \mathbf{y}_i (and subsequently \mathbf{y}_j) are vectors (of two elements) describing the crater centres

$$\mathbf{y}_i = [x_i, y_i]$$

Note ψ_i , x_i and y_i are values from the ellipse parameters that describe the crater rims.

Finally, σ is defined as

$$\sigma \approx \frac{0.85}{\sqrt{a_i b_i}} \sigma_{img}$$

Note, σ is only calculated for observed parameters (not for the reprojected) and σ_{img} represents the error in observed ellipse parameters.

A.1.7 Illustration of PECAN

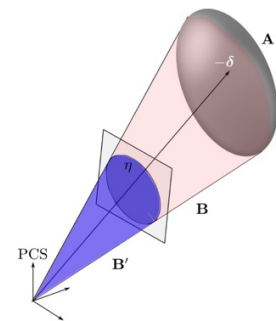
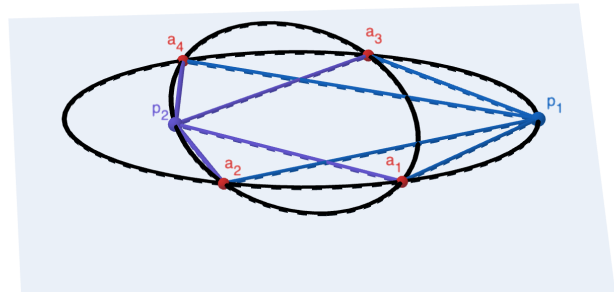


Figure A.1.7 PECAN estimation of camera pose [7]

In the illustration above, PECAN is used to solve for relative camera position δ by aligning the conics representing the projection of the ellipsoid A onto the ellipse η (denoted B) and the back-projection conic of ellipse η (denoted B').

A.1.8 Illustration of projective invariants for two coplanar craters



The illustration above shows the intersection of two ellipses corresponding to coplanar craters [2]. This intersection yields four points (which may be repeated or in the imaginary plane), for which two invariants may be calculated using the cross ratio of the four points to an arbitrary point on both conics [2].

A.2 Experimental Setup

A.2.1 Ellipse Parameterization

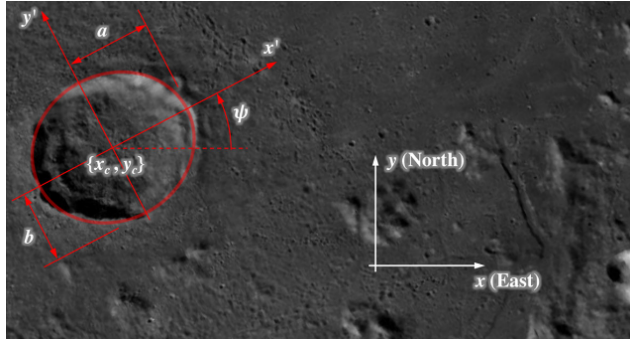


Figure A.2.1 Parametrization of an Ellipse [2]

The illustration above shows the parameterization of an ellipse (modelling a crater rim). The parameters x and y are the centre of the ellipse, a and b are the lengths of the semi-major and semi-minor axes and ψ is the rotation.

A.2.2 Estimated trajectory of CE5 landing

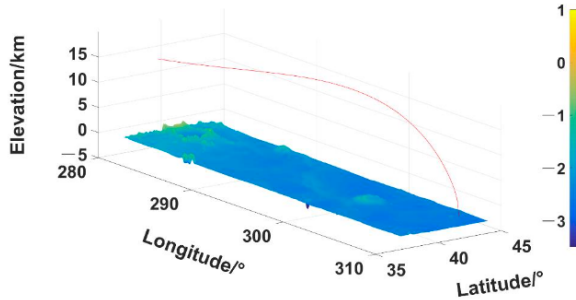


Figure A.2.2 Estimated descent trajectory of CE5 [11]

The illustration above shows the estimated trajectory of the CE5 landing.

A.2.3 Calculating the intrinsic matrix

We define our intrinsic matrix as $\mathbf{K} = \begin{bmatrix} f_{vx} & 0 & c_x \\ 0 & f_{vy} & c_y \\ 0 & 0 & 1 \end{bmatrix}$ [14]. We

do not calculate the centre of the image plane denoted by c_x and c_y , both parameters are given. However, we do calculate f_{vx} and f_{vy} which represent the field-of-view in degrees.

First, we convert a focal length (F) measured in mm into pixel focal lengths f_x and f_y [15]. This is achieved using the formula

$$f_x = \frac{F}{p_x}, f_y = \frac{F}{p_y}$$

Where p_x and p_y are the pixel sizes (width and height) in mm [15]. Then we convert f_x and f_y into f_{vx} and f_{vy} [14] using the following formulae:

$$f_{vx} = 2 \arctan\left(\frac{\text{image width}}{2 \times f_x}\right)$$

$$f_{vy} = 2 \arctan\left(\frac{\text{image height}}{2 \times f_y}\right)$$

Note that we use values $F = 15.4$ and $p_x = p_y = 0.0074$ attained from the National Astronomical Observatories Of China (NAOC) [12].

REFERENCES

- [1] "Chang'e 5." NASA.
<https://nssdc.gsfc.nasa.gov/nmc/spacecraft/display.action?id=2020-087A#:~:text=Chang%e%205%20is%20a,N%2C%2049%2D69%20deg> (accessed 6. Aug 2024).
- [2] J. A. Christian, H. Derksen, and R. Watkins, "Lunar Crater Identification in Digital Images," *The Journal of the Astronautical Sciences*, vol. 68, no. 4, pp. 1056-1144, Dec. 2021, doi: 10.1007/s40295-021-00287-8.
- [3] B. Maass, S. Woicke, W. M. Oliveira, B. Razgus, and H. Krüger, "Crater Navigation System for Autonomous Precision Landing on the Moon," *Journal of Guidance, Control, and Dynamics*, vol. 43, no. 8, pp. 1414-1431, 2020, doi: 10.2514/1.G004850.
- [4] M. Rodda. *Chang'e 5 Landing Camera Crater Detection Dataset*, Zenodo, Jun. 07, 2024. , doi: 10.5281/zenodo.11578934.
- [5] S. J. Robbins, "A New Global Database of Lunar Impact Craters >1–2 km: I. Crater Locations and Sizes, Comparisons With Published Databases, and Global Analysis," *Journal of Geophysical Research: Planets*, vol. 124, no. 4, pp. 871-892, 2019, doi: <https://doi.org/10.1029/2018JE005592>.
- [6] T. Kuga and H. Kojima, "Self-position estimation using terrain shadows for precise planetary landing," *Acta Astronautica*, vol. 148, pp. 345-354, Jul. 2018, doi: <https://doi.org/10.1016/j.actaastro.2018.05.002>.
- [7] C.-K. Chng, S. McLeod, M. Rodda, and T.-J. Chin, "Crater identification by perspective cone alignment," *Acta Astronautica*, vol. 224, pp. 1-16, Nov. 2024, doi: <https://doi.org/10.1016/j.actaastro.2024.07.053>.
- [8] M. Rodda, S. McLeod, K. Pham, and T.-J. Chin, *Camera-Pose Robust Crater Detection from Chang'e 5*. 2024.
- [9] W. Park, Y. Jung, H. Bang, and J. Ahn, "Robust Crater Triangle Matching Algorithm for Planetary Landing Navigation," *Journal of Guidance, Control, and Dynamics*, vol. 42, no. 2, pp. 402-410, 2019, doi: 10.2514/1.G003400.
- [10] G. Terzakis and M. Lourakis, "A Consistently Fast and Globally Optimal Solution to the Perspective-n-Point Problem," in *Computer Vision – ECCV 2020*, Cham, A. Vedaldi, H. Bischof, T. Brox, and J.-M. Frahm, Eds., 2020// 2020: Springer International Publishing, pp. 478-494.
- [11] P. Yang, Y. Huang, P. Li, S. Liu, Q. Shan, and W. Zheng, "Trajectory Determination of Chang'E-5 during Landing and Ascending," *Remote Sensing*, vol. 13, no. 23, doi: 10.3390/rs13234837.
- [12] *Chang'E-5 Landing Camera Level 2A scientific dataset*, doi: <https://dx.doi.org/10.12350/CLPDS.GRAS.CE5.LCAM-2A.vA>.
- [13] S. McLeod *et al.*, "Robust Perspective-n-Crater for Crater-based Camera Pose Estimation," in *2024 IEEE/CVF Conference on Computer Vision and Pattern Recognition Workshops (CVPRW)*, 17-18 June 2024 2024, pp. 6760-6769, doi: 10.1109/CVPRW63382.2024.00669.
- [14] "how to calculate field of view of the camera from camera intrinsic matrix?" stack overflow.
<https://stackoverflow.com/questions/39992968/how-to-calculate-field-of-view-of-the-camera-from-camera-intrinsic-matrix> (accessed 14. Oct 2024).
- [15] "How do I convert focal length from mm to pixels?" MathWorks.
<https://au.mathworks.com/matlabcentral/answers/10762-how-do-i-convert-focal-length-from-mm-to-pixels> (accessed 14. Oct 2024).